RESEARCH

Fabrication of pollution-free coal gangue-based catalytic material utilizing ferrous chloride as activator for efficient peroxymonosulfate activation

Zhiming Sun[1] · Xinlin Wang[1] · Shaoran Jia[1] · Jialin Liang[1] · Xiaotian Ning[1] · Chunquan Li[1,2]

Abstract

Novel coal gangue-based persulfate catalyst (CG-FeCl$_2$) was successfully synthesized by the means of calcinating under nitrogen atmosphere with the addition of ferrous chloride tetrahydrate (FeCl$_2$·4H$_2$O). The phase transformation of the prepared materials and gas products during the heating process are thoroughly investigated. It is suggested that ferrous chloride participated in the phase transformation and formed Si-O-Fe bonds. And the main gaseous products are H$_2$O, H$_2$, and HCl during the heating process. Besides, the ability of CG-FeCl$_2$ to activate peroxymonosulfate (PMS) for catalytic degradation of polycyclic aromatic hydrocarbons (PAHs) and phenol was deeply studied. More than 95% of naphthyl, phenanthrene and phenol were removed under optimizied conditions. In addition, ^{1}O$_2$, ·OH, and SO$_4^{·-}$ were involved in the CG-FeCl$_2$/PMS system from the free radical scavenging experiment, where ^{1}O$_2$ played a major role during the oxidation process. Furthermore, CG-FeCl$_2$/PMS system exhibited superior stability in a relatively wide pH range and the presence of common anion from related degradation experiments. Overall, the novel CG-FeCl$_2$ is an efficient and environmentally friendly catalyst, displaying potential application prospect in the field of PAHs and phenol-contaminated wastewater treatment.

Keywords Coal gangue · Persulfate activation · Advanced oxidation processes · Polycyclic aromatic hydrocarbons · Phenol · Ferrous chloride

1 Introduction

Coal gangue (CG) is a complex solid waste generated from coal mining and coal washing, whose major chemical composition is SiO$_2$ and Al$_2$O$_3$ with carbon content of 15%–30% (Li et al. 2010; Wu et al. 2021; Zhang et al. 2022). The accumulation of coal gangue not only occupies land resources but also results in serious environmental pollution (Sun et al. 2009). In particular, the residual element of C and S in the waste pile can spontaneously ignite, releasing many harmful gases like CO, CO$_2$, SO$_2$, H$_2$S, and NO$_x$ (Zhao et al. 2021). However, coal gangue could also be a useful source like heat energy, soil improvement, and (Al/Si/carbon)-based chemical products because of its high content of carbonaceous and clay minerals (Zhou et al. 2012; Li et al. 2023).

Moreover, coal mining and coal chemical can result in pollution of surface water and groundwater like ammonia nitrogen compounds, phenols and polycyclic aromatic hydrocarbons (PAHs) that are health-threatening and poor removal performance (Li and Zhang 2022; Mougnol et al. 2022; Wang et al. 2022). In particular, phenols (C$_6$H$_5$OH) and PAHs (two or more fused benzene ring molecules) are classified as priority pollutants. They are capable of undergoing bioaccumulating through food webs, and subsequently into humans (Zango et al. 2020). Therefore, it is necessary to comprehensive utilization of coal gangue and treat the (phenols and PAHs) contaminated wastewater flowing through mining areas.

A sub-category of advanced oxidation processes (AOPs), sulfate radical-based AOPs (SR-AOPs) have become a hotspot for the degradation of recalcitrant pollutants due to the long half-life (30–40 μs) and their selectivity to electron-rich moieties (Giannakis et al. 2021). Among the activation

✉ Chunquan Li
chunquanli@cumtb.edu.cn

[1] School of Chemical and Environmental Engineering, China University of Mining and Technology (Beijing), Beijing 100083, China

[2] Key Laboratory of Coal Processing and Efficient Utilization, (China University of Mining and Technology), Ministry of Education, Xuzhou 221116, China

without energy input, SO_4^{2-} can be easily generated by the transition metals activation of peroxymonosulfate (PMS) (Ahn et al. 2019; Zhang et al. 2021a, 2021b) since its unsymmetrical structure and large O–O bond length (Kohantorabi et al. 2021). However, transition metals are practically limited by their relatively high cost and potential secondary leaching pollution. Thus, the development of efficient catalyst without secondary pollutants is imminent (Song and Liu 2018; Li et al. 2020).

In previous studies, carbon-based materials including (reduced) graphene oxides (Sun et al. 2012), carbon nanotubes (Duan et al. 2015), and activated carbons (Huang et al. 2016) are promising metal-free candidates for PMS activation, which would solve the secondary pollutants of transition metals. However, the above-mentioned efficient carbonaceous materials suffer from high preparation costs and complicated preparation procedures. Thus, it is highly desirable to develop some novel carbon-based materials with distinct activation mechanisms that are more suitable for practical applications (Xu et al. 2020). To date, coal gangue based material-$ZnCl_2$ (CGM-$ZnCl_2$) (Li et al. 2022) and algae-derived boron-doped biochar (Hung et al. 2022), have been applied in activating PMS for phenol and PAHs removal, respectively.

In the present contribution, we efficiently utilized the carbon and silicon aluminum skeleton within coal gangue to prepare a novel and more efficient PMS catalyst for naphthyl, phenanthrene, and phenol removal than CGM-$ZnCl_2$ (82.6% degradation rate of phenol in 25 min) with negligible heavy metal leaching. Not only taking advantage of coal gangue but also attaining the clean treatment of wastewater. We further explored the phase transition and gas product of CG + $FeCl_2 \cdot 4H_2O$ mixture during the heating process by XRD and TG-FTIR-MS, respectively, which has not been researched to our knowledge. And we also identify the reactive oxygen species (ROS) by integrating several strategies. This study is dedicated to the mechanistic study of PMS activation over coal gangue-based catalysts for the removal of organic contaminants in wastewater.

2 Experimental

2.1 Materials

Ferrous chloride tetrahydrate ($FeCl_2 \cdot 4H_2O$), sodium dihydrogen phosphate (NaH_2PO_4), tertiary-butyl alcohol (TBA, $C_4H_{10}O$) were purchased from Xilong Chemical Co., Ltd (Guangzhou, China). Potassium peroxymonosulfate (PMS, $2KHSO_5 \cdot KHSO_4 \cdot K_2SO_4$) were purchased from Maya Reagent Co. (Zhejiang, China). L-histidine ($C_6H_9N_3O_2$), furfuryl alcohol (FFA, $C_5H_6O_2$), sodium chloride (NaCl), and phenol (C_6H_6O) were purchased from Aladdin Industrial

Corporation. Sodium bicarbonate ($NaHCO_3$) were purchased from Beijing Reagent Co. (Beijing, China). Methanol (MeOH, CH_3OH) were purchased from Macklin Biochemical Co., Ltd (Shanghai, China). The coal gangue with the fixed carbon content of 16.7% was obtained from Tunlan City, Shanxi Province. All chemicals were used without further purification.

2.2 Composites preparation

The coal gangue (CG) was first broken and ground to 100–200 mesh. Then 4.0 g of coal gangue and a certain amount of ferrous chloride tetrahydrate were mixed and dispersed in 15 mL deionized water, and the magnetic stirrer was used to impregnate the reaction at room temperature for 3 h. The mixture was dried overnight at 80 °C and ground. Finally, the mixture was placed in a tubular furnace and calcined in a nitrogen (N_2) atmosphere at 750 °C for 90 min with a heating rate of 10 °C/min. The influence of ferrous chloride tetrahydrate amount on sample preparation was investigated, including the mass ratio of CG to $FeCl_2 \cdot 4H_2O$ was 4:1, 4:1.5, 4:2, 4:3, and 4:4. The prepared materials were denoted as CG-$FeCl_2$(4:1), CG-$FeCl_2$(4:1.5), CG-$FeCl_2$(4:2), CG-$FeCl_2$(4:3) and CG-$FeCl_2$(4:4), respectively.

2.3 Characterization

X-ray powder diffraction (XRD) was recorded with the range of 2θ from 5° to 80°. X-ray fluorescence (XRF) was applied to analyze the chemical composition of the CG and CG-$FeCl_2$(4:2). Scanning electron microscopy (SEM), high-resolution transmission electron microscopy (HRTEM), and selected area electron diffraction (SAED) were employed to observe the morphologies and microstructure of the CG and CG-$FeCl_2$ materials. Thermogravimetric (TG) under N_2 atmosphere and thermogravimetric analyzer coupled with fourier transform infrared and mass spectrometry (TG-FTIR-MS) under an Ar atmosphere were applied to the analysis of weight changing and gas products during the heating process. The pore structure parameters of the as-prepared samples were obtained by using multipoint N_2 adsorption/desorption isotherm with the methods of BET and BJH. Fourier transformed infrared (FTIR) spectroscopy was recorded with the scanning range from 400 to 4000 cm^{-1}. Raman spectroscopy was employed to detect surface structure changes in CG and CG-$FeCl_2$(4:2). X-ray photoelectron spectroscopy (XPS) was performed to the analysis of surface chemical states of the CG-$FeCl_2$(4:2) material. Inductively coupled plasma-optical emission spectrometry (ICP-OES) was used to analyze the Fe leaching of CG-$FeCl_2$(4:2). Total Organic Carbon (TOC) was applied to the analysis of TOC removal efficiency in the degradation process. Electron paramagnetic resonance (EPR) spectroscopy was performed to identify the

reactive oxygen species (ROS) involved in the CG-FeCl$_2$/PMS system. The reaction products and potential reaction pathways of naphthyl/phenanthrene/phenol were revealed by a high-performance liquid chromatography-mass spectrometer (LC-MS).

2.4 Evaluation of catalytic activity

In a typical experiment, 60 mg of CG-FeCl$_2$(4:X) were dispersed into 30 mL of phenol solution (20.0 mg/L). The suspension was stirred for 30 min to achieve the adsorption-desorption equilibrium. Subsequently, 2.0 mL of PMS solution (30 mmol/L) was added to the above suspension. At desired time intervals, 0.5 mL of suspension was sampled and mixed with 0.5 mL of methanol to end the reaction, and then filtrated by a 0.22 µm filter.

The residual concentration of phenol was evaluated on a HPLC (LC-2030 C Shimadzu, Japan) with a C18 reverse-phase column (4.6 mm × 250 mm, 5 µm). The mobile phase was composed of acetonitrile (50%) and ultrapure water (50%) with a flow rate of 1.0 mL/min. The injection volume was 20 µL and the detection wavelength was 254 nm.

3 Results and discussion

3.1 Characterization of catalysts

The XRD patterns of the CG and prepared CG-FeCl$_2$ composites are shown in Fig. 1a. The XRD pattern of CG showed the obvious characteristic peak at 26.64°, which corresponds to the (011) lattice of quartz (JCPDS No.85-0798). Meanwhile, the characteristic peaks at 12.38° and 33.05° in the XRD pattern of CG can be assigned to the (001) of kaolinite (JCPDS No.80-0886) and (200) lattice of pyrite (JCPDS No.71-1680), respectively. As for the prepared CG-FeCl$_2$ composites, the characteristic peaks of kaolinite and pyrite disappeared, while the characteristic peaks of iron sulfide (JCPDS No.65-0408), sekaninaite (JCPDS No.54-0679), mullite (JCPDS No.15-0776) and aluminum iron silicon (JCPDS No.45-1205) appeared, meaning that phase transition has appeared during the heating process.

Furthermore, the phase transition of main component of CG including pyrite, kaolinite, coal (for studying the carbon in CG), and their phase transformation products after adding FeCl$_2$·4H$_2$O are discovered through changes in the XRD patterns as shown in Fig. 1b. The XRD pattern of pyrite-FeCl$_2$(4:2) showed the presence of pyrrhotite (JCPDS No.29-0725), which was owing to the partial decomposition of the pyrite (Oliveira et al. 2018). However, for the prepared CG-FeCl$_2$ composites as displayed in Fig. 1a, only CG-FeCl$_2$ (4:1) appeared with the characteristic peak at 43.50°, which may be owing to the (2012) reflection of crystalline pyrrhotite. While other CG-FeCl$_2$ composites appear a characteristic peak at around 43.22°, which is due to the (102) reflection of crystalline iron sulfide.

Meanwhile, the XRD profiles of coal showed the peak at 20° < 2θ < 30°, which corresponds to the (002) reflection of carbon due to the stacking structure of aromatic layers (Takagi et al. 2004). While the XRD pattern of coal-FeCl$_2$ (4:2) showed the peaks at 43.20°, 43.60° and 44.70°, which corresponded to the (102) lattice of iron sulfide, (2012)
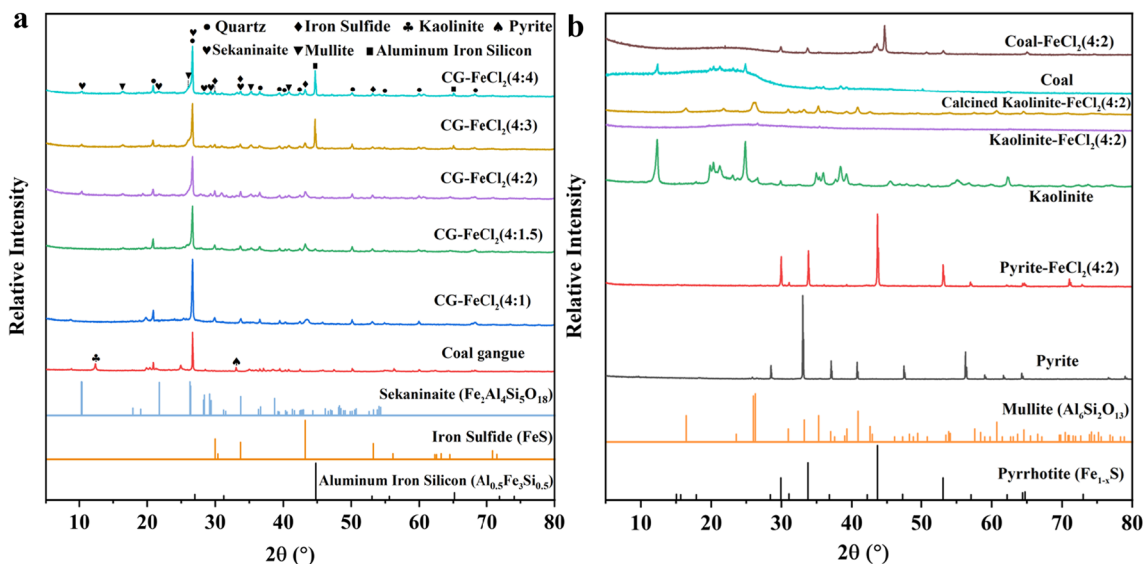
Fig. 1 XRD patterns of **a** CG and the prepared CG-FeCl$_2$ composites **b** Pyrite, Pyrite-FeCl$_2$(4:2), Kaolinite, Kaolinite-FeCl$_2$(4:2), Calcined Kaolinite-FeCl$_2$(4:2), Coal and Coal-FeCl$_2$(4:2) composites

lattice of pyrrhotite (maybe owing to the S element in coal combined with the Fe from $FeCl_2 \cdot 4H_2O$), and (220) lattice of aluminum iron silicon, respectively (Fig. 1a). Moreover, X-ray diffractogram of the prepared kaolinite-$FeCl_2$ material doesn't show any kaolinite peak but the presence of a halo peak band at $18° < 2\theta < 25°$ indicated the formation of amorphous alumino-silicate phase (Elimbi et al. 2011). While the prepared CG-$FeCl_2$ (from 4:1.5 to 4:4) and calcined kaolinite-$FeCl_2$ material all showed the presence of mullite. Overall, the above XRD pattern difference between kaolinite-$FeCl_2$, CG-$FeCl_2$ composites, and calcined kaolinite-$FeCl_2$ may be due to the structural and impurity variations of kaolinite (Pask and Tomsia 1991). Besides, the results of HRTEM images and SAED pattern further proved the presence of mullite in the prepared CG-$FeCl_2$ materials

as presented in Figs. 2j-m. However, the formation temperature of mullite from kaolinite is normally 1000 °C, which was obviously reducd after the introduction of $FeCl_2 \cdot 4H_2O$. This is due to the iron could enter the lattice of mullite, affecting the morphology and reducing the temperature of mullite crystallization (Ilić et al. 2014; Ye et al. 2019).

Table 1 presents the chemical composition of CG and CG-$FeCl_2$ (4:2). The content of iron trioxide increases from 6.87 wt% for CG to 29.22 wt% for CG-$FeCl_2$ (4:2), which originated from pyrite and the $FeCl_2 \cdot 4H_2O$ activation. By combining the results of XRD (Fig. 1), FTIR (Fig. 4a), and XPS (Fig. 5c), it can be further confirmed that iron intercalated into the lattice during the activation process.

The SEM and HRTEM images illustrate the morphological characteristics of CG and CG-$FeCl_2$ samples.

Table 1 The chemical composition of CG and CG-$FeCl_2$(4:2) in wt%

Sample	SiO_2	Al_2O_3	Fe_2O_3	SO_3	K_2O	TiO_2	MgO	CaO	Na_2O	Others
CG	50.45	30.56	6.87	7.23	1.78	1.57	0.38	0.61	0.18	0.37
CG–FeCl_2 (4:2)	41.00	25.85	29.22	0.30	1.20	0.98	0.29	0.61	0.17	0.38
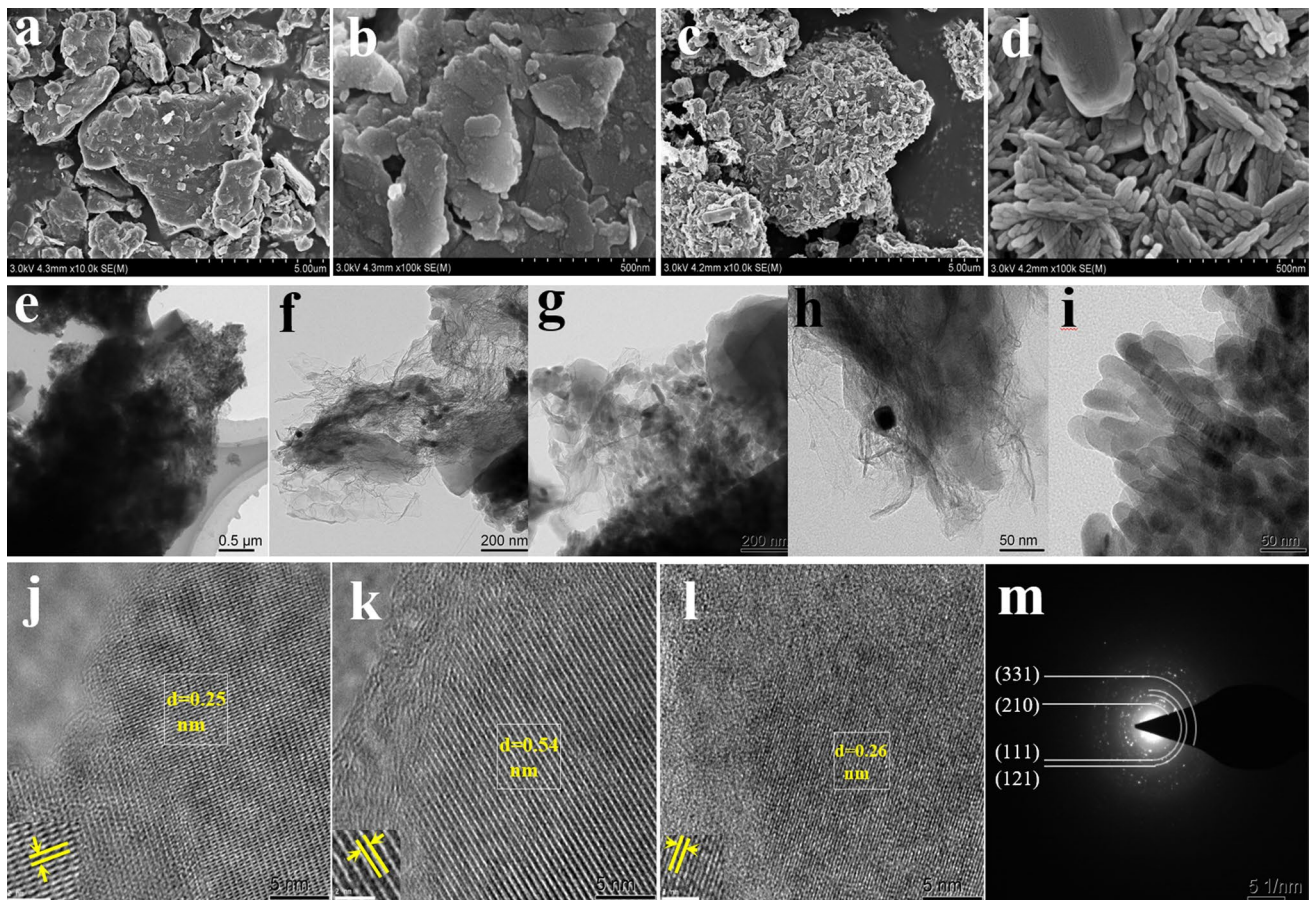
Fig. 2 SEM images of **a** and **b** Coal gangue, **c** and **d** CG-$FeCl_2$ composites, **e−l** HRTEM images of CG-$FeCl_2$ composites, **m** SAED pattern of CG-$FeCl_2$ composites

As presented in Figs. 2a–d, the CG displayed a typically smooth 2D lamellar structure (Sun et al. 2020). While for CG-FeCl$_2$ samples, their structure became porous with many irregular cylindrical particles, which may be caused by the dehydroxylation of kaolinite and phase change (Cao et al. 2016) during the heating process. Furthermore, the HRTEM images of CG-FeCl$_2$ material revealed the interplanar spacing of 0.25, 0.54, and 0.26 nm, which could be indexed to the (111), (110) lattice planes of mullite (Kong et al. 2003) and (512) lattice plane of sekaninaite, respectively. The crystalline structure of mullite could also be demonstrated by the diffraction rings observed from the corresponding SAED pattern of CG-FeCl$_2$ samples.

To further analyze the pore structure of CG and the CG-FeCl$_2$ composites derived from different activator (FeCl$_2$·4H$_2$O) amounts, the obtained N$_2$ adsorption-desorption isotherms and pore diameter distribution curves were shown in Fig. 3. The shapes of the isotherms indicate changes in pore size distribution (Lopez et al. 2013). As shown in Fig. 3a, the curve shape of CG showed a typical II isotherm (IUPAC classification) with probable pore diameter of 12.756 nm, which indicates the presence of nonporous and macro-porous structures. On the other hand, the CG-FeCl$_2$ composites all exhibit Type IV isotherm with the adsorption-desorption hysteresis loop, which indicates a combination of micropores and mesopores with the pore diameter ranging from 3.879 to 10.216 nm (Zhang et al. 2014).

The calculated structure parameters of a series of coal gangue-based materials, including specific surface area (SSA), total pore volume, and average pore diameter are summarized in Table 2. It can be deduced that the addition of activation agent FeCl$_2$·4H$_2$O can drastically increase the SSA (4.45 to 66.50 m^2/g) and total pore volume (0.014 to 0.084 cm^3/g) of CG by almost 15 and 6 times, respectively.

Table 2 BET surface area, pore volume, and average pore size of coal gangue and CG-FeCl$_2$ composites

Sample	S_{BET} (m^2/g)	Total pore volume (cm^3/g)	Average pore diameter (nm)
CG	4.45	0.014	12.8
CG–FeCl$_2$(4:1)	6.29	0.016	10.2
CG–FeCl$_2$(4:1.5)	39.62	0.038	3.9
CG–FeCl$_2$(4:2)	57.92	0.057	3.9
CG–FeCl$_2$(4:3)	66.50	0.073	4.4
CG–FeCl$_2$(4:4)	62.54	0.084	5.4

The change in SSA and total pore volume corresponds to a decrease in average pore diameter from 12.8 to 4.4–5.4 nm.

Moreover, the results in Fig. 3b and Table 2 suggested that the introduction of FeCl$_2$·4H$_2$O developed new mesopores during the mass ratio of CG/FeCl$_2$·4H$_2$O from 4:1 to 4:1.5. When the ratio ranged from 4:1.5 to 4:3, FeCl$_2$·4H$_2$O not only prompted the generation of mesopores but also enlarged existing pores, resulting in significant increases in SSA, total pore volume, and average pore diameter. However, when the ratio went up to 4:4, the SSA of CG-FeCl$_2$ decreased with the increased total pore volume and average pore diameter, which may be owing to its micropores being enlarged into mesopores (Qian et al. 2007). The above variation suggests that the amount of activation agent has a strong effect on the pore structure of CG-FeCl$_2$ materials, especially from 4:1 to 4:2. This is due to the generation of mesopores and the enlargement of existing pores, thus significantly altering the adsorption, migration, and catalytic degradation of materials against organic contaminant.

Figure 4a shows the FT-IR spectra of CG and the prepared CG-FeCl$_2$ materials. All the samples exhibited
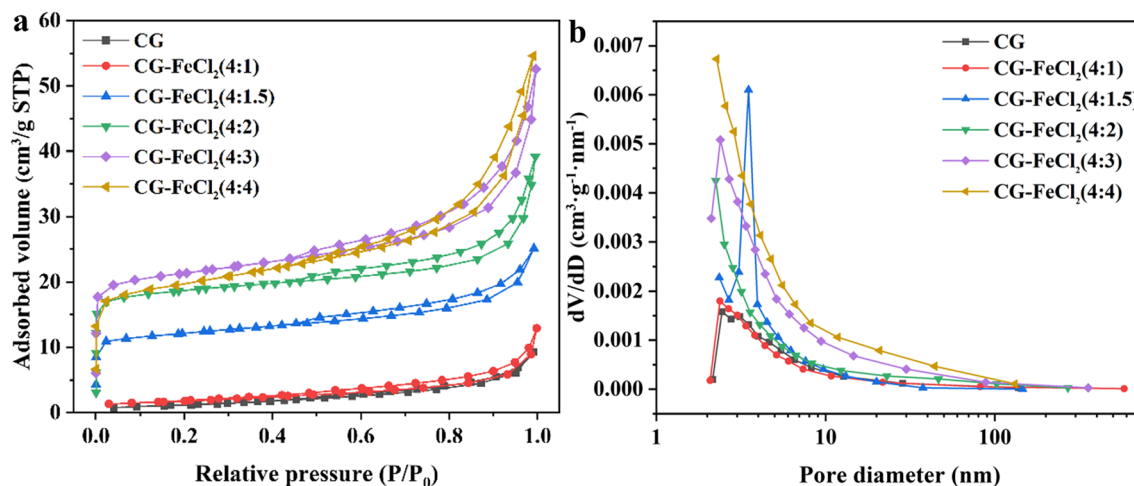
Fig. 3 **a** Adsorption/desorption isotherms and Pore size distribution plots of **b** CG and the prepared CG-FeCl$_2$ composites
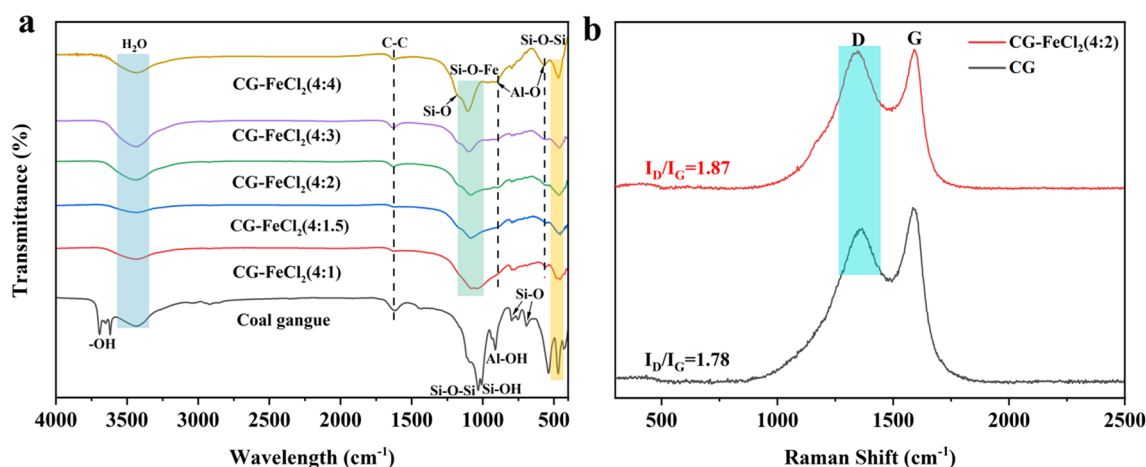
Fig. 4 **a** FT-IR spectra of CG and the prepared CG-FeCl$_2$ composites, **b** Raman spectra of CG and the CG-FeCl$_2$ (4:2) material

adsorption bands at $3442-3434$ cm^{-1}, $1632-1616$ cm^{-1}, $799-795$ cm^{-1}, and $471-457$ cm^{-1}, which corresponds to adsorbed H$_2$O, the C–C stretching vibrations of polyaromatic C＝C (Zhou et al. 2007), symmetric Si–O stretching vibration, and in-plane Si–O–Si bending vibration within SiO$_4$ tetrahedra, respectively (Zhang et al. 2011). For CG, the adsorption bands at 935/913 cm^{-1} and 539 cm^{-1} represent the Al-OH and Al-O-Si bending vibrations, respectively (Zhu et al. 2016). The changes between the FTIR spectrum of CG and the prepared CG-FeCl$_2$ materials can be attributed to the activation of FeCl$_2$.4H$_2$O and the heating process. Especially, the characteristics peak of Si-O-Si shifted from 1033 cm^{-1} for CG to $1107-1081$ cm^{-1} for CG-FeCl$_2$ materials. These are mainly ascribed to the formation of Si-O-Fe bonds since the coupling of silicon with iron (Zhang et al. 2021a, 2021b), which is consistent with the results of XRD and XPS. Besides, the adsorption bands at around 1180, 900 and 570 cm^{-1} represent the Si-O and Al-O bending vibrations, respectively, and they were corresponding to the spectrum of mullite (Yoshida et al. 2010), which prove the presence of it in the prepared CG-FeCl$_2$ material again. Finally, bending vibrations of C＝O and C-O may be covered by the adsorption bands at $1690-1550$ cm^{-1} (C–C) and 1107–1081 cm^{-1} (Si–O–Fe).

Figure 4b shows the Raman spectra of CG and the prepared CG-FeCl$_2$(4:2) material. Among the spectra, well-known D and G bands were observed near 1350 and 1585 cm^{-1}, respectively. The ratio of the intensities of the disorder-induced D band to the symmetry-allowed G band ratio (I_D/I_G) has been used to characterize the defect density in carbon materials (Escribano et al. 2001; Saito et al. 2011). The value of I_D/I_G was higher for CG-FeCl$_2$(4:2) (1.87) than that of CG (1.78), indicating that the CG-FeCl$_2$(4:2) material possess more structural disorder (amorphousness) compared with CG (Sreńscek-Nazzal et al. 2016), enabling

CG-FeCl$_2$(4:2) to exhibit a higher level of reaction possibility, thereby enhancing activities of CG-FeCl$_2$ for PMS activation (Wang et al. 2020).

Furthermore, the surface chemical states of the CG-FeCl$_2$(4:2) composite were identified by XPS analysis as shown in Fig. 5. The survey scan of both fresh and used CG-FeCl$_2$(4:2) (Fig. 5a) appeared the characteristic peaks of C 1s, O 1s, Si 2p, Al 2p, and Fe 2p. In the C 1s spectra (Fig. 5b), the deconvoluted peaks at 284.5, 286.0, 287.3, 288.9, and 291.0 eV in the fresh spectrum as well as 284.4, 286.0, 287.3, 288.9 and 291.2 eV in the used spectrum can be assigned to C–C, C–O, C＝O, O＝C–O bonds and adsorbed (CO and CO$_2$), respectively (Fen-rong et al. 2011; Chen et al. 2020). In the O 1s spectra (Fig. 5c), the deconvoluted peaks at 531.5, 532.0, 533.0, and 533.8 eV can be assigned to Al–O/C＝O, Si–O–Fe, Si–O, and O＝C–O bonds, respectively (Figueiredo et al. 2011; Wang et al. 2018; Hu et al. 2021). In the Fe 2p spectra (Fig. 5d), the fitted peaks at 710.9 and 724.3 eV in the fresh spectrum as well as 711.1 and 724.3 eV in the used spectrum assigned to Fe^{3+} (Yamashita and Hayes 2008), indicating that Fe^{3+} is the main valence state in CG-FeCl$_2$(4:2). Owing to the slow transformation of Fe^{3+} back to Fe^{2+}, it is implied that Fe in CG-FeCl$_2$(4:2) has little effect on PMS activation.

The thermal behavior (50 to 750 °C) of CG, CG + 50% FeCl$_2$·4H$_2$O, and FeCl$_2$·4H$_2$O at the heating rate of 10 °C/min under an inert atmosphere was performed through thermogravimetry and differential scanning calorimetry (TG-DSC). As displayed in Fig. 6, CG + 50% FeCl$_2$·4H$_2$O has three stages of mass loss. The first two stages were around 50 to 135 °C and 135 to 190 °C, respectively, which both can be attributed to the evolution of H$_2$O and H$_2$ (Fig. 7a), corresponding to the heat absorption peaks at 130 and 180 °C on its DSC curve. The difference between these two stages is the type of water, including the physically absorbed moisture
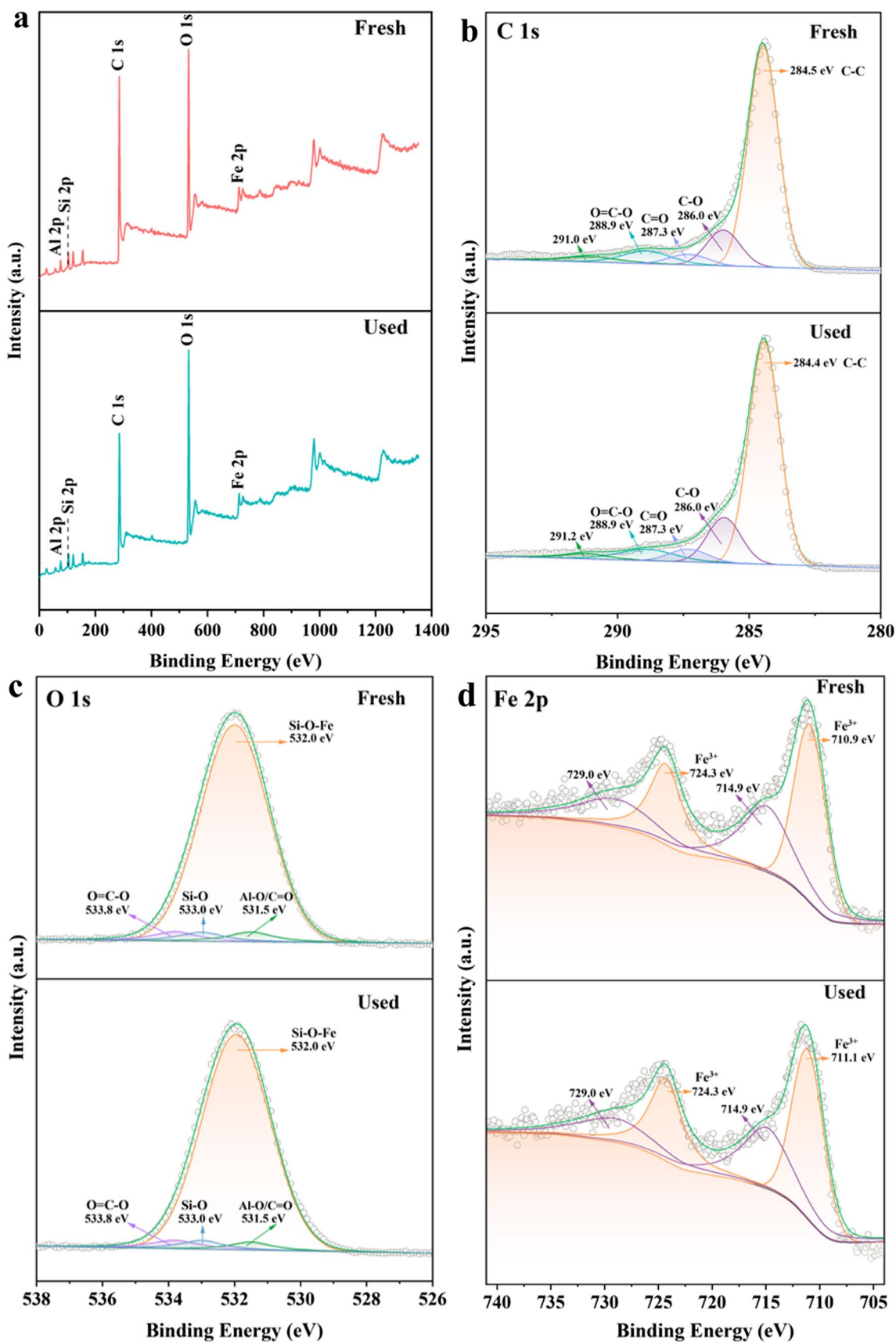
Fig. 5 XPS spectra of **a** survey, **b** C 1s, **c** O 1s, **d** Fe 2p for fresh and used CG-FeCl$_2$(4:2) material
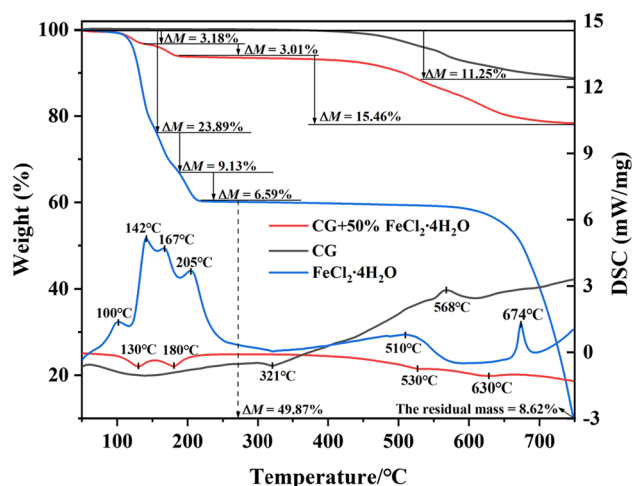
Fig. 6 TG-DSC curves of the CG, CG + 50% FeCl$_2$·4H$_2$O (the mass ratio of CG to FeCl$_2$·4H$_2$O was 4:2), FeCl$_2$·4H$_2$O

and the decomposition of FeCl$_2$·4H$_2$O (Bi et al. 2021). The third stage (around 335 to 750 °C) coincides with the dissociation of molecules (kaolinite and organic matter etc.) (Zhou et al. 2012) and the release of volatiles including H$_2$, HCl, and Cl (Fig. 7a and c), corresponding to the heat absorption peaks at 530 and 630 °C on its DSC curve. Thus, the dehydroxylation of kaolinite (Al$_2$O$_3$·2SiO$_2$·2H$_2$O) in coal gangue transformed to the crystalized mullite (Al$_2$O$_3$·2SiO$_2$) (Cao et al. 2016) occurrence in 400 to 750 °C can be drawn. Besides, considering the difference between TG-DSC results of CG + 50% FeCl$_2$·4H$_2$O and FeCl$_2$·4H$_2$O, especially around 600 to 750 °C. The conclusion can be proved again that the element of Fe is mostly retained after the heating process, which is consistent with the results of XRF (Fe$_2$O$_3$ from 6.87 wt% to 29.22 wt%), FTIR and XPS (the formation of Si-O-Fe bonds).

Furthermore, the MS and FTIR investigation of the volatile products evolved during TG measurements (TG-MS-FTIR) offered overall thermal behavior of CG + 50% FeCl$_2$·4H$_2$O mixture under an inert atmosphere, as displayed in Figs. 7a–d. The standard FTIR spectra of H$_2$O, HCl, and CO from the National Institute of Standards and Technology (NIST) (Chu et al. 1999) were displayed in Fig. 7e as well. The MS signal for the M/Z = 18 of H$_2$O$^+$ and M/Z = 17 of HO$^+$ have similar evolution patterns in the 50–750 °C (Fig. 7a). Therefore, we can safely consider that HO$^+$ was mainly resulted from H$_2$O$^+$ splitting. Besides, the evolution of H$_2$ can be divided into two main stages. In the first stage, at 50–300 °C, H$_2$ was resulted from water splitting. The second stage was above 400 °C, H$_2$ comes from the condensation of (hydro) aromatic or the decomposition of substrate abundant in hydrogen and heterocyclic compounds (Wang et al. 2013). As shown in Fig. 7b, even though the M/Z = 28 of CO$^+$ has one peak at 67 °C, the typical bands at

2178 and 2114 cm^{-1} were not detected in Fig. 7d, thus the evolution of CO didn't take place in the heating process. It is noticeable that there is no peak for the M/Z = 32 of O$_2$$^+$ and M/Z = 44 of CO$_2$$^+$ (Fig. 7b), suggesting an almost insulated oxygen heating environment, which induced the results of FTIR (the rupture of C-C bonds) and Raman (I$_D$/I$_G$) was higher for CG-FeCl$_2$(4:2) (1.87) than that of CG (1.78). As shown in Fig. 7c, HCl is formed in the temperature ranges (above 485 °C rather than begin at 83 °C), which is similar to the peak of CO$^+$ at 67 °C. Because HCl treatment can increase the pore volume and openness of coal samples (Yi et al. 2021), the evolution of HCl played a positive role in changing the pore structure of CG-FeCl$_2$. In addition, HCl is hazardous, and placing the outlet of the gas in water during the synthesis process can avoid harm to the human body to some extent.

FTIR analysis was helpful to distinguish the evolution stages of the volatile products of CG + 50% FeCl$_2$·4H$_2$O mixture. The characteristic peaks of H$_2$O appeared at 100 °C and gradually strengthened at 100 to 550 °C and kept stable at 550 to 750 °C (Fig. 7c). Meanwhile, the bands at around 2944 and 2798 cm^{-1} for HCl had peaks above 500 °C. The characteristic peaks of HCl gradually strengthened at 550~600 °C and gradually weakened at 650 to 750 °C, which is agreement with the third mass loss stage of CG + 50% FeCl$_2$·4H$_2$O mixture (Fig. 6). Besides, there are three kinds of oxygen-containing functional groups at 500 to 750 °C, i.e. OH-ether O hydrogen bond, cyclic OH and C–O (from phenols, alcohols, and ethers), which is located near 3265, 3180 and 1188 cm^{-1}, respectively (Scaccia 2013; Yue et al. 2021).

Overall, the synthesis process from CG + 50% FeCl$_2$·4H$_2$O mixture to CG-FeCl$_2$(4:2) has occurred the following changes: (1) Phase transition and chemical composition: The principal component of coal gangue includes kaolinite, pyrite, and carbon. After the activation process, the crystalline phase of kaolinite and pyrite disappear, while the characteristic peaks of iron sulfide, sekaninaite, mullite, and aluminum iron silicon appear. Moreover, the content of Fe$_2$O$_3$ from 6.87 wt% for coal gangue increased to 29.22 wt% for CG-FeCl$_2$(4:2); (2) Evolved gases and pore structure: The volatilization of H$_2$O, H$_2$, and HCl leads to the weight loss of CG + 50% FeCl$_2$·4H$_2$O mixture, which has played an important role in the changing of the pore structure of the synthesized material as well (Yi et al. 2021; Gao et al. 2022); (3) Chemical bond features: The rupture of the C–C bond, more defects, electron-rich C=O groups, and the formation of Si–O–Fe bonds lead to an efficient and environmentally friendly catalyst.

3.2 Catalytic activity of catalysts

The catalytic performance of CG and the prepared CG-FeCl$_2$ materials were evaluated through the degradation
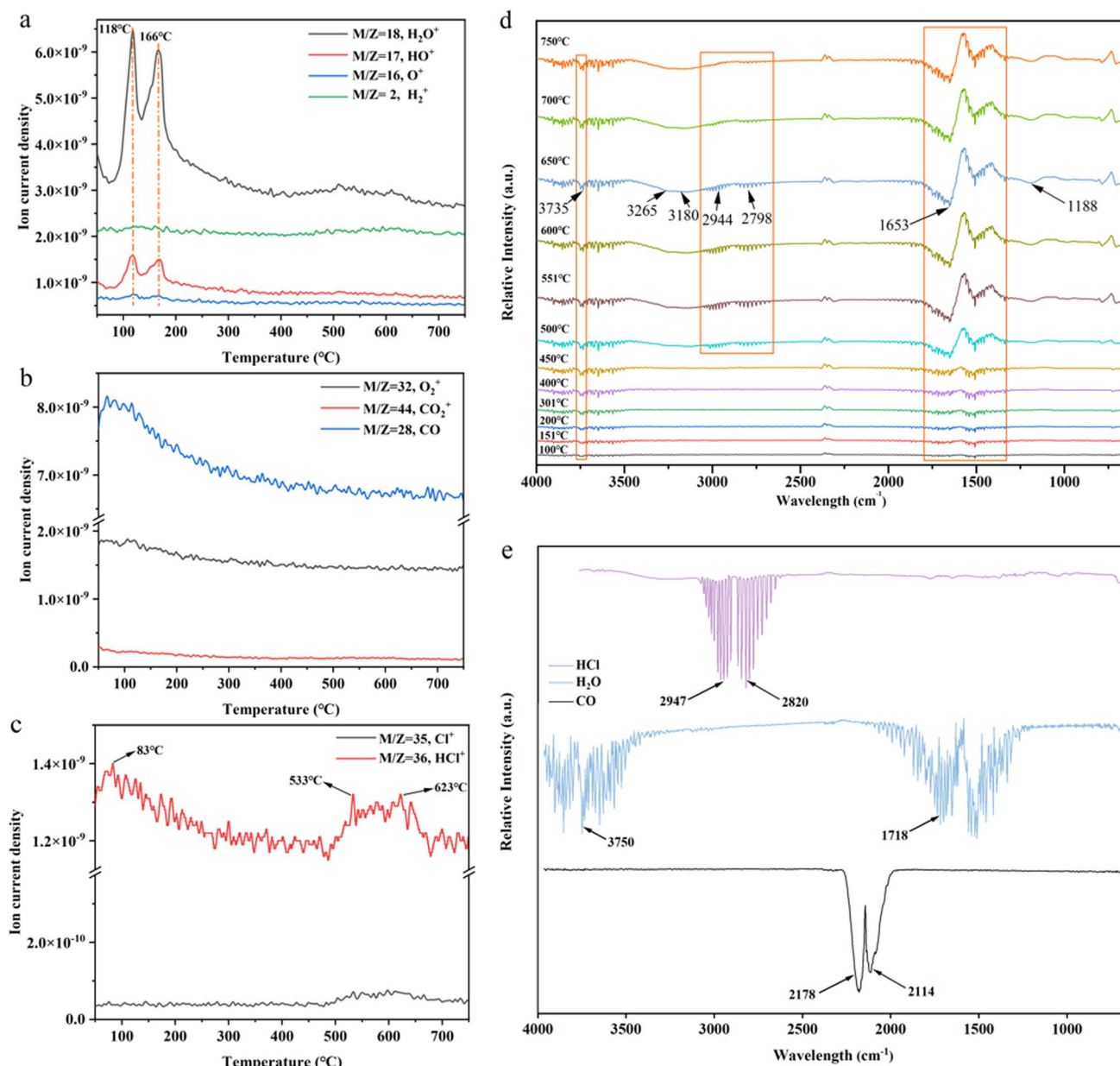
Fig. 7 Evolution of **a–c** MS curves **d** FTIR spectra during TG analysis of CG + 50% FeCl$_2$·4H$_2$O mixture under Ar-pyrolysis at 50 to 750 °C **e** Standard FTIR spectra of HCl, H$_2$O, and CO from NIST

of phenol under the same conditions. As can be seen from Fig. 8a, CG, CG-FeCl$_2$(4:1), and CG-FeCl$_2$(4:1.5) did not have a satisfactory performance due to a lack of adsorption capacity and low PMS activation ability for oxidizing phenol. In contrast, CG-FeCl$_2$(4:2), CG-FeCl$_2$(4:3), and CG-FeCl$_2$(4:4) could oxidize phenol with a degradation percentage of 95%, 96%, and 100% within 25 min, indicating that they could efficiently form ROS through PMS activation. Because the phenol degradation efficiency was consistent with the mass ratio of CG to FeCl$_2$·4H$_2$O. Hereupon, the mass ratio of 4:2 was chosen as the optimum

dosage for the following experiments considering the cost and economy.

The pseudo-first-order kinetic pattern can be expressed as -Ln(C/C_0) = kt, where C is the concentration of phenol at instant t, C_0 is the initial phenol concentration, k presents the kinetic rate constant, and t is the time of reaction. The k results of phenol degradation on CG and some selected CG-FeCl$_2$ composites were displayed in Fig. 8b. The k (0.06469 min^{-1}) value of CG-FeCl$_2$(4:2) was nearly 45 times higher than that of CG (0.00143 min^{-1}), giving the superior generation rate of ROS in CG-FeCl$_2$(4:2)/
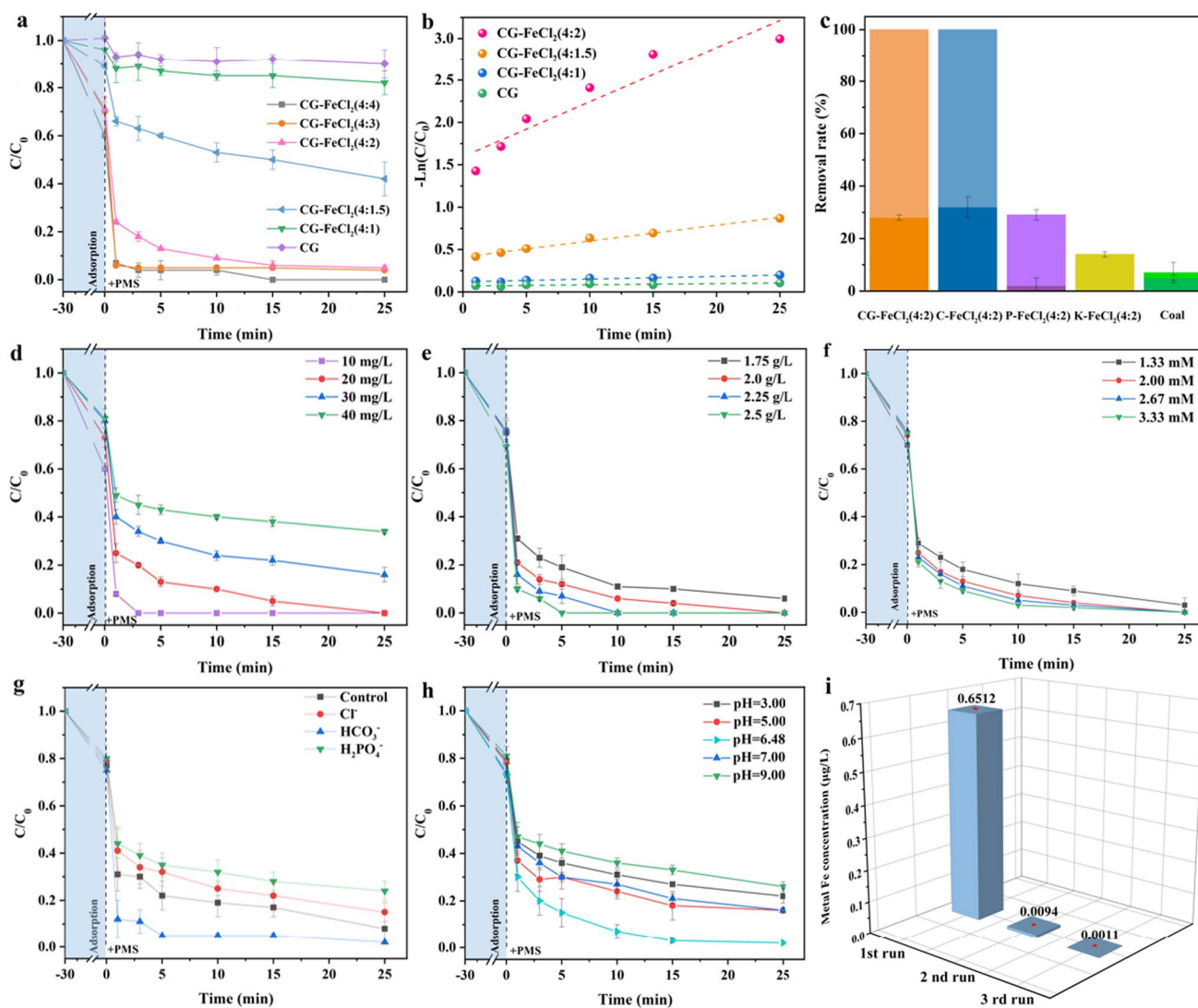
Fig. 8 The removal of phenol (**a**) and linear transform $\ln(C_0/C)$ of the kinetic curves of phenol (**b**) with CG and the prepared CG-FeCl$_2$ composites, **c** phenol removal with CG-FeCl$_2$(4:2), Coal-FeCl$_2$(4:2), Pyrite-FeCl$_2$(4:2), Kaolinite-FeCl$_2$(4:2) and Coal, **d** The effect of phenol concentration, **e** effect of catalyst dosage, **f** effect of PMS con- centration, **g** effect of anions-50 mM, **h** effect of pH on the removal of phenol; **i** Fe leaching concentration of CG-FeCl$_2$(4:2) during the degradation process. General conditions: C_0 (phenol) = 20 mg/L, C_0 (catalyst) = 2.0 g/L, C_0 (PMS) = 2.00 mM, V = 30 mL, initial pH = 6.48, temperature = 293 K

PMS system. Moreover, the influence of coal (for study- ing the carbon), pyrite (Rahimi et al. 2021) and kaolinite (Li et al. 2019) (both have been applied to PMS activation) in coal gangue was considered for CG-FeCl$_2$/PMS system. Figure 8c depicts phenol degradation in various materi- als including CG-FeCl$_2$(4:2), coal-FeCl$_2$(4:2), pyrite- FeCl$_2$(4:2), kaolinite-FeCl$_2$(4:2) and coal. Among them, CG-FeCl$_2$(4:2) and coal-FeCl$_2$(4:2) could oxidize phenol completely after 25 min. However, pyrite-FeCl$_2$(4:2), kaolinite-FeCl$_2$(4:2) and coal only attain 29%, 14% and 7% removal percentage of phenol, respectively. Therefore, the FeCl$_2\cdot$4H$_2$O activated carbon component within coal gangue as well as the introduced variable-valence iron play

an important role for phenol removal in the CG-FeCl$_2$/ PMS system.

The effect of phenol concentration, catalyst dosage, and PMS concentration was considered in the CG-FeCl$_2$(4:2)/ PMS system. As can be seen from Fig. 8d, the degradation efficiency of phenol by CG-FeCl$_2$(4:2)/PMS depends on the initial concentration of phenol. Complete phenol removal can be achieved at phenol concentrations of 10 and 20 mg/L, while phenol removal efficiency decreased to 84% and 66% at phenol concentrations of 30 and 40 mg/L, respectively. The phenomenon may be owing to the mutual competition of phenol for ROS and a higher organic load under the same amount of PMS.

It is believed that phenol degradation depended on catalyst dosage in the CG-FeCl$_2$(4:2)/PMS system as well. Figure 8e shows phenol degradation at various catalyst dosages ranging from 1.75 to 2.5 g/L. The complete degradation is observed at 2.25 and 2.5 g/L of CG-FeCl$_2$(4:2) in 10 min, while in the same duration at catalyst dosages of 1.75 and 2.0 g/L, the phenol removal percentage reached 89% and 94%, respectively. The enhanced degradation efficiency of phenol was due to the more active sites under same organic load (Zeng et al. 2020; Madihi-Bidgoli et al. 2021).

PMS concentration is also a variable influencing phenol degradation, which is representative of the amounts of free radicals generated in SR-AOPs (Saputra et al. 2013). As displayed in Fig. 8f, phenol degradation efficiencies were > 90% at PMS concentrations between 1.33 and 3.33 mM, suggesting the great catalytic efficiency of CG-FeCl$_2$(4:2)/PMS system. Besides, the removal of phenol was faster with the PMS concentration of 3.33 mM than other lower PMS concentrations, which can be ascribed to that more radicals could be formed within unit time (Zhang et al. 2022).

The effect of anions ($H_2PO_4^-$, Cl^-, and HCO_3^-) on the degradation of phenol in the CG-FeCl$_2$(4:2)/PMS system was also investigated (Fig. 8g). The removal efficiency increased with the introduction of HCO_3^-, which might be attributed to that HCO_3^- could activate PMS to generate active species for degrading phenol (Yang et al. 2010; Wang and Wang 2020). However, the removal of phenol was suppressed in the background of $Cl^-/H_2PO_4^-$. Because both $\cdot OH$ and $SO_4^{\cdot-}$ can react with $Cl^-/H_2PO_4^-$ to generate the lower reaction efficiency radical of $Cl^{\cdot}$, $PO_4^{\cdot2-}$, $HPO_4^{\cdot-}$, and $H_2PO_4^{\cdot}$. Compared with $H_2PO_4^-$, the lower suppression effect of Cl^- on the degradation of phenol may be owing to $Cl^{\cdot}$ only formed under acid conditions in the presence of $\cdot OH$ (Wang and Wang 2021).

Since the value of pH can directly influence catalytic activity, the degradation of phenol in the CG-FeCl$_2$(4:2)/PMS system in terms of pH (from 3 to 9) was studied as well. As shown in Fig. 8h, CG-FeCl$_2$(4:2) displayed efficient degradation of phenol over a pH range from 5 to 7 (removal percentage > 84%), whereas the degradation of phenol decreased at pH = 3 and 9. The phenomenon is due to the H-bond between H^+ and the O–O group of PMS would be more significant in a strong acid environment, while at the pH of 9, the self-decomposition of PMS initiated, resulting in the decreased degradation efficiency (Wang et al. 2017). Overall, CG-FeCl$_2$(4:2)/PMS system exhibits good performance (removal percentage > 74%) in the pH range from 3 to 9, suggests it is favorable for treating wastewater in weak acid and weak base conditions.

Furthermore, the Fe leaching of CG-FeCl$_2$(4:2) in the phenol degradation process was studied by ICP-OES analysis (Fig. 8i). The amount of Fe concentrations for CG-FeCl$_2$(4:2) catalyst in the water after 3 cycles was 0.6512 µg/L, 0.0094 µg/L, and 0.0011 µg/L, respectively, which confirms negligible Fe leaching compared with Chinese Surface Water Environmental Quality Standard (GB 3838 − 2002, the standard value of Fe is 0.3×10^3 µg/L). Moreover, since Fe is the only one major heavy metal element in CG-FeCl$_2$(4:2) (Table 1), the security of it for practical application was proved by results of ICP-OES.

To quantify the mineralization efficiency of phenol, the removal of TOC for this degradation process was determined (Fig. 9a). The TOC removal value of 66% was achieved within 1 min, suggesting fast mineralization of phenol in the CG-FeCl$_2$(4:2)/PMS system. Moreover, the removal value of TOC is 78% after 25 min. Thus, we can consider that intermediate compounds are produced and phenol can be efficiently degraded and mineralized in the CG-FeCl$_2$/PMS
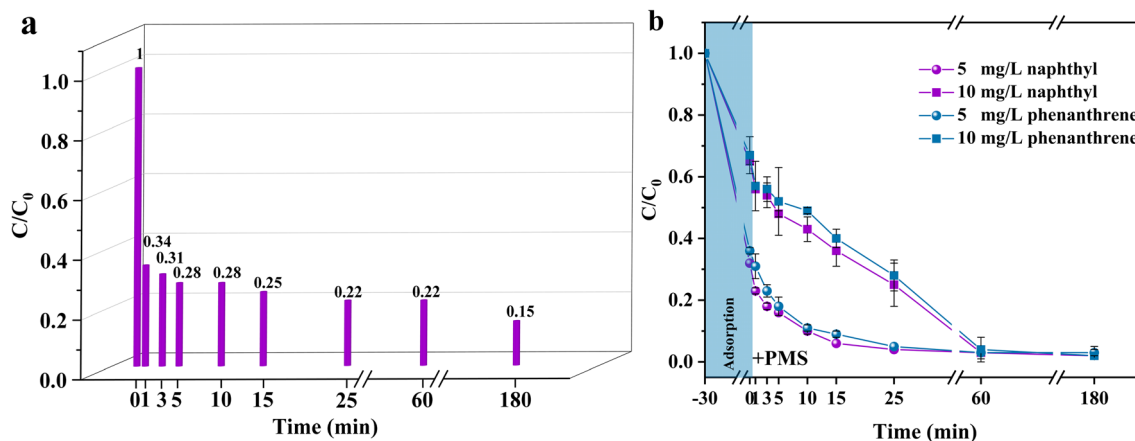
Fig. 9 a The TOC removal efficiency of phenol and **b** The removal efficiency of naphthyl and phenanthrene in the CG-FeCl$_2$(4:2)/PMS system. General conditions: C_0 (phenol) = 20 mg/L, C_0 (naphthyl) = 5 and 10 mg/L, C_0 (phenanthrene) = 5 and 10 mg/L, C_0 (catalyst) = 2.0 g/L, C_0 (PMS) = 2.00 mM, V = 30 mL, temperature = 293 K

system. To investigate the removal efficiency of PAHs in the CG-FeCl$_2$(4:2)/PMS system, the degradation experiments of naphthyl and phenanthrene were conducted (Fig. 9b). High naphthyl (97%) and phenanthrene (96%) removal percentages can be achieved at their concentrations of 5 and 10 mg/L after 60 min of reaction. Therefore, we can safely consider that CG-FeCl$_2$(4:2)/PMS system can also be applied in the degradation of PAHs.

3.3 Reaction mechanism and degradation pathways

To confirm that CG-FeCl$_2$(4:2) or PMS cannot directly remove phenol alone, related experiments were conducted. As shown in Fig. 10a, the removal percentages of phenol only reach 19% in the CG-FeCl$_2$ system and 7% in the PMS system. The result suggesting that ROS are mainly generated from the catalytic effect of CG-FeCl$_2$(4:2) on PMS.

To identify involved reactive oxygen species (ROS) during the degradation process, related experiments were conducted in the presence of L-histidine and furfuryl alcohol (FFA) (scavenger of $^1O_2$), tertiary butanol (TBA, scavenger of $\cdot OH$), and methanol (MeOH, scavenger of $\cdot OH$ and $SO_4^{\cdot -}$) (Yang et al. 2020). The removal efficiency decreased following the trend of L-histidine > FFA > TBA > MeOH (Fig. 10b), suggesting that $^1O_2$ are the main species that contribute to the degradation of phenol in the presence of PMS. In addition, TBA and MeOH showed inhibitory effect with a phenol degradation percentage of 57% and 82%, respectively. This confirms that both $\cdot OH$ and $SO_4^{\cdot -}$ radicals show some responsibility for the degradation of phenol in the CG-FeCl$_2$/PMS system.

To further confirm the generation of ROS, electron paramagnetic resonance (EPR) with 5,5-dimethyl-1-pyrroline-N-oxide (DMPO) and 2,2,6,6-tetramethyl-4-piperidinyloxyl (TEMP) as spin trapping agents was employed to capture radicals produced in the CG-FeCl$_2$/PMS system. Characteristic signals of $\cdot OH$, $SO_4^{\cdot -}$, and $^1O_2$ were observed in the CG-FeCl$_2$/PMS system (Fig. 10(c-d). In addition, the signal intensity of $\cdot OH$, $SO_4^{\cdot -}$ and $^1O_2$ continually increased along with time, indicating that CG-FeCl$_2$ can continuously activate PMS to form ROS (Zhang et al. 2021a, 2021b). While
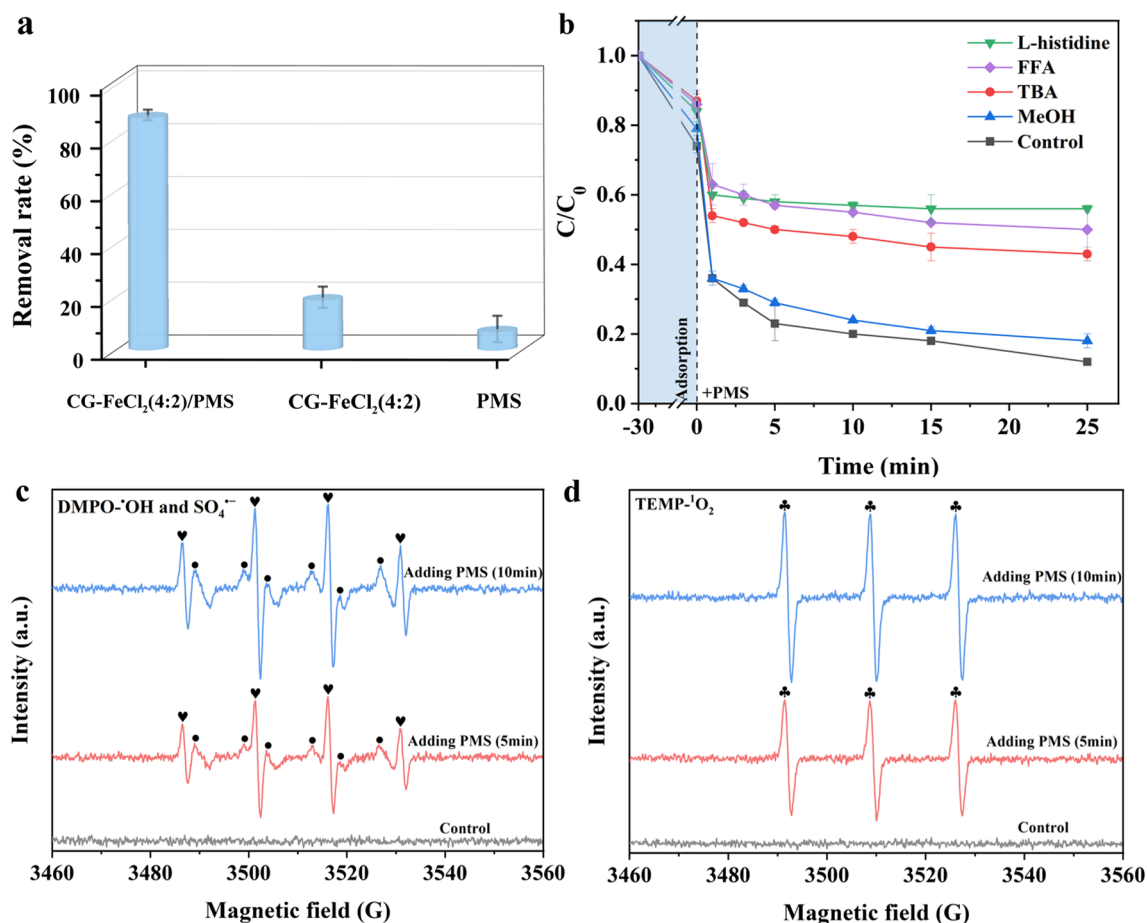
Fig. 10 The Removal of phenol in **a** Different systems **b** The presence of L-histidine (5 mM), furfuryl alcohol (FFA, 5 mM), tertiary butanol (TBA, 500 mM), and methanol (MeOH, 500 mM), electron paramagnetic resonance spectra of **c** $\cdot OH$ and $SO_4^{\cdot -}$, **d** $^1O_2$ over CG-FeCl$_2$ material

in the CG-FeCl$_2$ alone system, no signals for $^.$OH, SO$_4$$^{.-}$, and ^{1}O$_2$ were observed, indicating that ROS was generated from CG-FeCl$_2$ activation of PMS. These results agree well with the above experiments, together confirming that all of ^{1}O$_2$, $^.$OH, and SO$_4$$^{.-}$ radicals show responsibility for the degradation of phenol in the CG-FeCl$_2$/PMS system.

We further investigated the intermediates of naphthyl, phenanthrene, and phenol degradation in the GC-FeCl$_2$/PMS system by LC-MS. Two possible pathways of naphthyl, phenanthrene, and phenol were proposed based on recognized intermediates in the GC-FeCl$_2$/PMS system, as shown in Figs. 11a–c.

Based on all the above results, the efficient degradation of phenol in the CG-FeCl$_2$/PMS system was proposed and summarized as followed: CG-FeCl$_2$ materials have larger specific surface area, pore volume, and smaller pore size compared to that of CG, which leads to better adsorption ability for PMS and phenol, eventually speeding up the process of PMS activation to form highly reactive complexes

(part 1); The defects in CG-FeCl$_2$ can promote the transfer of electrons from phenol to activate PMS and elongate the O-O bond of PMS (HSO$_5$$^-$) to generate $^.$OH and SO$_4$$^{.-}$, which also have strong reactivity with aromatic compounds like phenol (part 2) (Duan et al. 2016). In addtion, the low oxygen content of CG-FeCl$_2$ materials are beneficial to the oxidation of organic contanminants in PMS system, and electron-rich C=O groups in them are the critical reactive sites via direct electron transfer and the generation of ^{1}O$_2$ or cleave PMS into $^.$OH and SO$_4$$^{.-}$ (part 3) (Wang et al. 2020; Huang et al. 2021) (Fig. 12).

4 Conclusions

To synthesize novel carbon-based materials and efficient utilization of coal gangue towards catalytic oxidation of organic contanminants in wastewater, the catalyst CG-FeCl$_2$ is developed in this study. The introduction of activator FeCl$_2$·4H$_2$O
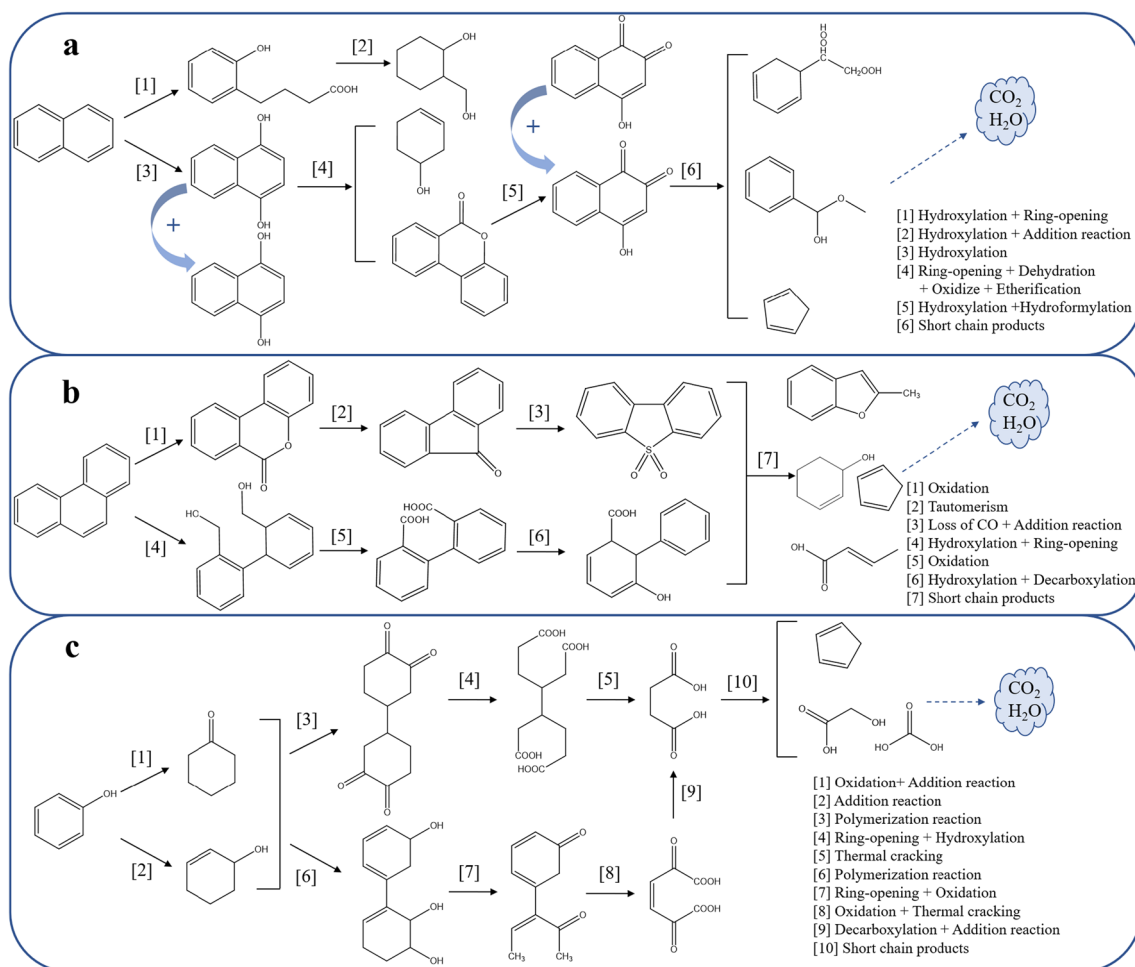
Fig. 11 a The potential degradation pathways of naphthyl **b** Phenanthrene, and **c** phenol in CG-FeCl$_2$/PMS system. General conditions: C_0 (phenol) = 20 mg/L, C_0 (naphthyl) = 10 mg/L, C_0 (phenanthrene) = 10 mg/L, C_0 (catalyst) = 2.0 g/L, C_0 (PMS) = 2.00 mM, V = 30 mL, temperature = 293 K
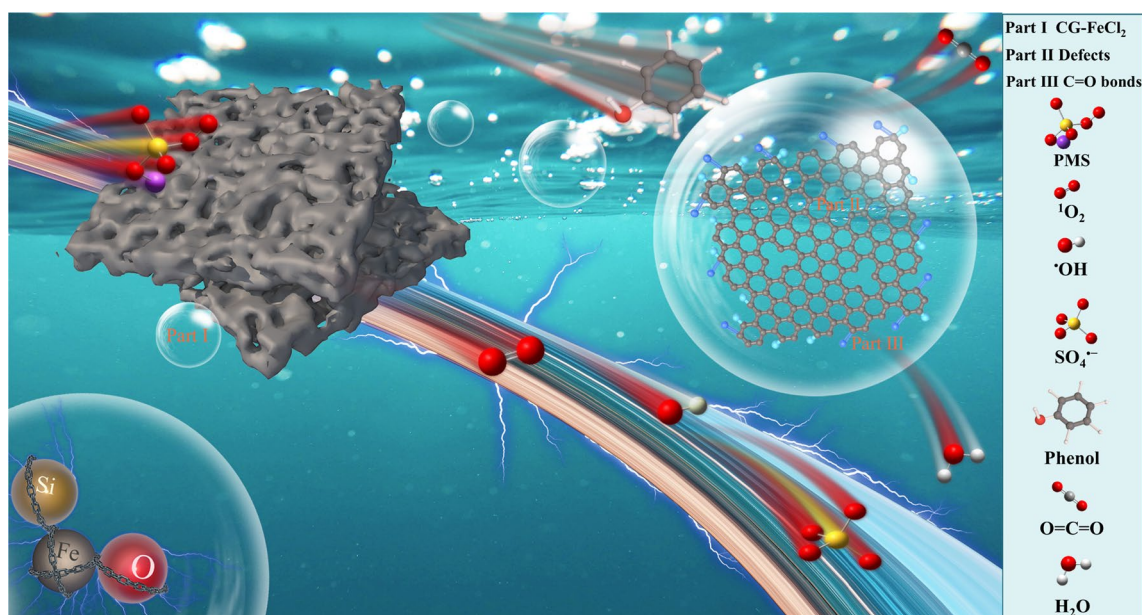
Fig. 12 The diagram of the possible degradation mechanism of phenol in the CG-FeCl₂/PMS system

participated in the phase transformation and formed the Si–O–Fe bonds. And the main gaseous products including H_2O, H_2, and HCl during the heating process was proved by various characterizations. The resulting CG-FeCl₂ catalyst shows excellent peroxymonosulfate catalytic activity in the removal of naphthyl, phenanthrene and phenol ($\geq 95\%$) under optimized conditions. This unique catalytic oxidation activity is mainly due to the synergetic effect of pore structure, defects, and electron-rich $C=O$ groups. From the scavenging experiments, multiple active oxygen species including $\cdot OH$, $SO_4^{\cdot -}$ and $^1O_2$ are generated in the CG-FeCl₂/PMS system, and the significance order was $^1O_2 > \cdot OH > SO_4^{\cdot -}$. Through the analysis of CG-FeCl₂/PMS/(naphthyl/phenanthrene/phenol) system by LC-MS, the potential degradation pathways of naphthyl, phenanthrene, and phenol were obtained as well. This work provides a feasible solution for the preparation of pollution-free coal gangue-based catalysts for the removal of PAHs and phenol.

Declarations

Conflict of interest There are no conflicts of interest to declare.

References

Ahn Y, Bae H, Kim H, Kim S, Kim J, Lee S, Lee J (2019) Surface-loaded metal nanoparticles for peroxymonosulfate activation: efficiency and mechanism reconnaissance. Appl Catal B 241:561–569

Bi H, Wang C, Lin Q, Jiang X, Jiang C, Bao L (2021) Pyrolysis characteristics, artificial neural network modeling and environmental impact of coal gangue and biomass by TG-FTIR. Sci Total Environ 751:142293

Cao Z, Cao Y, Dong H, Zhang J, Sun C (2016a) Effect of calcination condition on the microstructure and pozzolanic activity of calcined coal gangue. Int J Miner Process 146:23–28

Chen X, Wang X, Fang D (2020) A review on C1s XPS-spectra for some kinds of carbon materials. Fullerenes Nanotubes and Carbon Nanostructures 28(12):1048–1058

Chu PM, Guenther FR, Rhoderick GC, Lafferty WJ (1999) The NIST quantitative infrared database. J Res Natl Inst Stand Technol 104(1):59

Duan X, Sun H, Wang Y, Kang J, Wang S (2015) N-doping-induced nonradical reaction on single-walled carbon nanotubes for catalytic phenol oxidation. ACS Catal 5(2):553–559

Duan X, Ao Z, Zhou L, Sun H, Wang G, Wang S (2016) Occurrence of radical and nonradical pathways from carbocatalysts for aqueous and nonaqueous catalytic oxidation. Appl Catal B 188:98–105

Elimbi A, Tchakoute HK, Njopwouo D (2011) Effects of calcination temperature of kaolinite clays on the properties of geopolymer cements. Constr Build Mater 25(6):2805–2812

Escribano R, Sloan JJ, Siddique N, Sze N, Dudev T (2001) Raman spectroscopy of carbon-containing particles. Vib Spectrosc 26(2):179–186

Fen-rong L, Wen L, Hui-qing G, Bao-qing L, Zong-qing B, Rui-sheng H (2011) XPS study on the change of carbon-containing groups and sulfur transformation on coal surface. J Fuel Chem Technol 39(2):81–84

Figueiredo NM, Carvalho N, Cavaleiro A (2011) An XPS study of au alloyed Al–O sputtered coatings. Appl Surf Sci 257(13):5793–5798

Gao S, Jia L, Zhou Q, Cheng H, Wang Y (2022) Microscopic pore structure changes in coal induced by a CO_2-H_2O reaction system. J Petrol Sci Eng 208:109361

Giannakis S, Lin KA, Ghanbari F (2021) A review of the recent advances on the treatment of industrial wastewaters by Sulfate Radical-based Advanced oxidation processes (SR-AOPs). Chem Eng J 406:127083

Hu Y, Li X, Wang G, Luo F, Yi K, Iradukunda Y, Shi G (2021) Biomass carbon materials derived from starch and their electrochemical properties. Int J Electrochem Sci 16:210359–210370

Huang Z, Bao H, Yao Y, Lu J, Lu W, Chen W (2016) Key role of activated carbon fibers in enhanced decomposition of pollutants using heterogeneous cobalt/peroxymonosulfate system. J Chem Technol Biotechnol 91(5):1257–1265

Huang W, Xiao S, Zhong H, Yan M, Yang X (2021) Activation of persulfates by carbonaceous materials: a review. Chem Eng J 418:129297

Hung C, Chen C, Huang C, Cheng J, Dong C (2022) Algae-derived metal-free boron-doped biochar as an efficient bioremediation pretreatment for persistent organic pollutants in marine sediments. J Clean Prod 336:130448

Ilić S, Zec S, Miljković M, Poleti D, Pošarac-Marković M, Janaćković D, Matović B (2014) Sol–gel synthesis and characterization of iron doped mullite. J Alloys Compd 612:259–264

Kohantorabi M, Moussavi G, Giannakis S (2021) A review of the innovations in metal-and carbon-based catalysts explored for heterogeneous peroxymonosulfate (PMS) activation, with focus on radical vs. non-radical degradation pathways of organic contaminants. Chem Eng J 411:127957

Kong XY, Wang ZL, Wu J (2003) Rectangular single-crystal Mullite Microtubes. Adv Mater 15(17):1445–1449

Li Y, Zhang X (2022) Characterization of the health and irrigation risks and hydrochemical properties of groundwater: a case study of the Selian coal mine area, Ordos, Inner Mongolia. Appl WATER Sci 12(10):236

Li C, Wan J, Sun H, Li L (2010) Investigation on the activation of coal gangue by a new compound method. J Hazard Mater 179(1–3):515–520

Li C, Huang Y, Dong X, Sun Z, Duan X, Ren B, Zheng S, Dionysiou DD (2019) Highly efficient activation of peroxymonosulfate by natural negatively-charged kaolinite with abundant hydroxyl groups for the degradation of atrazine. Appl Catal B 247:10–23

Li J, Zhu J, Fang L, Nie Y, Tian N, Tian X, Lu L, Zhou Z, Yang C, Li Y (2020) Enhanced peroxymonosulfate activation by supported microporous carbon for degradation of tetracycline via non-radical mechanism. Sep Purif Technol 240:116617

Li C, Wang S, Zhang X, Wu J, Zheng S, Sun Z (2022) In-situ preparation of coal gangue-based catalytic material for efficient peroxymonosulfate activation and phenol degradation. J Clean Prod 374:133926

Li X, Shao J, Zheng J, Bai C, Zhang X, Qiao Y, Colombo P (2023) Fabrication and application of porous materials made from coal gangue: a review. Int J Appl Ceram Technol 20:2099–2124

Lopez FA, Centeno TA, Garcia-Diaz I, Alguacil FJ (2013) Textural and fuel characteristics of the chars produced by the pyrolysis of waste wood, and the properties of activated carbons prepared from them. J Anal Appl Pyrol 104:551–558

Madihi-Bidgoli S, Asadnezhad S, Yaghoot-Nezhad A, Hassani A (2021) Azurobine degradation using Fe_2O_3@ multi-walled carbon nanotube activated peroxymonosulfate (PMS) under UVA-LED irradiation: performance, mechanism and environmental application. J Environ Chem Eng 9(6):106660

Mougnol J, Waanders F, Fosso-Kankeu E, Al Alili AR (2022) Leaching of Polycyclic aromatic hydrocarbons from the coal tar in sewage wastewater, acidic and alkaline mine drainage. Int J Environ Res Public Health 19(8):4791

Oliveira EMD, Oliveira CMD, Sala MVB, Montedo ORK, Peterson M (2018) Thermal behavior of pyrite in the CO_2 and N_2 atmosphere for obtaining pyrrhotite: A magnetic material. Mater Res. https://doi.org/10.1590/1980-5373-MR-2017-0244

Pask JA, Tomsia AP (1991) Formation of mullite from sol-gel mixtures and kaolinite. J Am Ceram Soc 74(10):2367–2373

Qian Q, Machida M, Tatsumoto H (2007) Preparation of activated carbons from cattle-manure compost by zinc chloride activation. Bioresour Technol 98(2):353–360

Rahimi F, van der Hoek JP, Royer S, Javid A, Mashayekh-Salehi A, Sani MJ (2021) Pyrite nanoparticles derived from mine waste as efficient catalyst for the activation of persulfates for degradation of tetracycline. J Water Process Eng 40:101808

Saito R, Hofmann M, Dresselhaus G, Jorio A, Dresselhaus MS (2011) Raman spectroscopy of graphene and carbon nanotubes. Adv Phys 60(3):413–550

Saputra E, Muhammad S, Sun H, Wang S (2013) Activated carbons as green and effective catalysts for generation of reactive radicals in degradation of aqueous phenol. RSC Adv 3(44):21905–21910

Scaccia S (2013) TG–FTIR and kinetics of devolatilization of Sulcis coal. J Anal Appl Pyrol 104:95–102

Song X, Liu M (2018) Advanced treatment of biotreated coking wastewater with peroxymonosulfate oxidation catalyzed by granular activated carbon. J Chem Technol Biotechnol 93(8):2191–2198

Sreńscec-Nazzal J, Narkiewicz U, Morawski AW, Wróbel R, Gęsikiewicz-Puchalska A, Michalkiewicz B (2016) Modification of commercial activated carbons for CO2 adsorption. Acta Physica Polonica, A. 129(3):394–401

Sun YZ, Fan JS, Qin P, Niu HY (2009) Pollution extents of organic substances from a coal gangue dump of Jiulong Coal Mine, China. Environ Geochem Health 31(1):81–89

Sun H, Liu S, Zhou G, Ang HM, Tadé MO, Wang S (2012) Reduced graphene oxide for catalytic oxidation of aqueous organic pollutants. ACS Appl Mater Interfaces 4(10):5466–5471

Sun Z, Zhang X, Dong X, Liu X, Tan Y, Yuan F, Zheng S, Li C (2020) Hierarchical assembly of highly efficient visible-light-driven Ag/g-C_3N_4/kaolinite composite photocatalyst for the degradation of ibuprofen. J Materiomics 6(3):582–592

Takagi H, Maruyama K, Yoshizawa N, Yamada Y, Sato Y (2004) XRD analysis of carbon stacking structure in coal during heat treatment. Fuel 83(17–18):2427–2433

Wang J, Wang S (2020) Reactive species in advanced oxidation processes: formation, identification and reaction mechanism. Chem Eng J 401:126158

Wang J, Wang S (2021) Effect of inorganic anions on the performance of advanced oxidation processes for degradation of organic contaminants. Chem Eng J 411:128392

Wang S, Tang Y, Schobert HH, Guo YN, Gao W, Lu X (2013) FTIR and simultaneous TG/MS/FTIR study of late Permian coals from Southern China. J Anal Appl Pyrol 100:75–80

Wang G, Chen S, Quan X, Yu H, Zhang Y (2017) Enhanced activation of peroxymonosulfate by nitrogen doped porous carbon for effective removal of organic pollutants. Carbon 115:730–739

Wang Z, Peng B, Zhang L, Zhao Z, Liu D, Peng N, Wang D, He Y, Liang Y, Liu H (2018) Study on formation mechanism of fayalite (Fe_2SiO_4) by solid state reaction in sintering process. Jom 70(4):539–546

Wang J, Duan X, Gao J, Shen Y, Feng X, Yu Z, Tan X, Liu S, Wang S (2020) Roles of structure defect, oxygen groups and heteroatom doping on carbon in nonradical oxidation of water contaminants. Water Res 185:116244

Wang YJ, Zhang QR, Liu MT, Liu H, Chen YY, Hu XD (2022) Simulation and dynamic control of removal phenols from coal gasification wastewater by synergistic extraction. SEPARATION AND PURIFICATION TECHNOLOGY 285

Wu J, Yan X, Li L, Gu J, Zhang T, Tian L, Su X, Lin Z (2021) High-efficiency adsorption of cr (VI) and RhB by hierarchical porous carbon prepared from coal gangue. Chemosphere 275:130008

Xu L, Wu C, Liu P, Bai X, Du X, Jin P, Yang L, Jin X, Shi X, Wang Y (2020) Peroxymonosulfate activation by nitrogen-doped biochar from sawdust for the efficient degradation of organic pollutants. Chem Eng J 387:124065

Yamashita T, Hayes P (2008) Analysis of XPS spectra of Fe^{2+} and Fe^{3+} ions in oxide materials. Appl Surf Sci 254(8):2441–2449

Yang S, Wang P, Yang X, Shan L, Zhang W, Shao X, Niu R (2010) Degradation efficiencies of azo dye Acid Orange 7 by the interaction of heat, UV and anions with common oxidants: persulfate, peroxymonosulfate and hydrogen peroxide. J Hazard Mater 179(1–3):552–558

Yang L, Chen Y, Ouyang D, Yan J, Qian L, Han L, Chen M, Li J, Gu M (2020) Mechanistic insights into adsorptive and oxidative removal of monochlorobenzene in biochar-supported nanoscale zero-valent iron/persulfate system. Chem Eng J 400:125811

Ye H, Li Y, Sun J, Sun Y, Wu X, Yan M (2019) Novel iron-rich mullite solid solution synthesis using fused-silica and α-Al_2O_3 powders. Ceram Int 45(4):4680–4684

Yi M, Cheng Y, Wang C, Wang Z, Hu B, He X (2021) Effects of composition changes of coal treated with hydrochloric acid on pore structure and fractal characteristics. Fuel 294:120506

Yoshida K, Hyuga H, Kondo N, Kita H (2010) Synthesis of precursor for fibrous mullite powder by alkoxide hydrolysis method. Mater Sci Engineering: B 173(1–3):66–71

Yue W, MO W, GONG W, WEI X, Xing F, ZHANG S (2021) Functional groups of sequential extracts and corresponding residues from Hefeng sub-bituminous coal based on FT-IR analysis. J Fuel Chem Technol 49(7):890–901

Zango ZU, Sambudi NS, Jumbri K, Ramli A, Abu Bakar NHH, Saad B, Rozaini MNH, Isiyaka HA, Osman AM, Sulieman A (2020) An overview and evaluation of highly porous adsorbent materials for polycyclic aromatic hydrocarbons and phenols removal from wastewater. Water 12(10):2921

Zeng Z, Khan A, Wang Z, Zhao M, Mo W, Chen Z (2020) Elimination of atrazine through radical/non-radical combined processes by manganese nano-catalysts/PMS and implications to the structure-performance relationship. Chem Eng J 397:125425

Zhang N, Liu X, Sun H, Li L (2011) Pozzolanic behaviour of compound-activated red mud-coal gangue mixture. Cem Concr Res 41(3):270–278

Zhang Y, Xing Z, Duan Z, Li M, Wang Y (2014) Effects of steam activation on the pore structure and surface chemistry of activated carbon derived from bamboo waste. Appl Surf Sci 315:279–286

Zhang W, Qian L, Chen Y, Ouyang D, Han L, Shang X, Li J, Gu M, Chen M (2021a) Nanoscale zero-valent iron supported by attapulgite produced at different acid modification: synthesis mechanism and the role of silicon on cr (VI) removal. Chemosphere 267:129183

Zhang LS, Jiang XH, Zhong ZA, Tian L, Sun Q, Cui YT, Lu X, Zou JP, Luo SL (2021b) Carbon Nitride supported High-Loading Fe single-Atom Catalyst for activation of Peroxymonosulfate to Generate $^1O_2$ with 100% selectivity. Angew Chem Int Ed 60(40):21751–21755

Zhang X, Liu Y, Li C, Tian L, Yuan F, Zheng S, Sun Z (2022) Fast and lasting electron transfer between γ-FeOOH and g-C_3N_4/kaolinite containing N vacancies for enhanced visible-light-assisted peroxymonosulfate activation. Chem Eng J 429:132374

Zhao Y, Qiu J, Ma Z, Sun X (2021) Eco-friendly treatment of coal gangue for its utilization as supplementary cementitious materials. J Clean Prod 285:124834

Zhou J, Sui Z, Zhu J, Li P, Chen D, Dai Y, Yuan W (2007) Characterization of surface oxygen complexes on carbon nanofibers by TPD, XPS and FT-IR. Carbon 45(4):785–796

Zhou C, Liu G, Yan Z, Fang T, Wang R (2012) Transformation behavior of mineral composition and trace elements during coal gangue combustion. Fuel 97:644–650

Zhu X, Zhu Z, Lei X, Yan C (2016) Defects in structure as the sources of the surface charges of kaolinite. Appl Clay Sci 124:127–136